

Article

Surface Fluorination for the Stabilization in Air of Garnet-Type Oxide Solid Electrolyte for Lithium Ion Battery

Michael Herraiz ¹, Saida Moumen ¹, Kevin Lemoine ¹ , Laurent Jouffret ¹ , Katia Guérin ¹ , Elodie Petit ¹ , Nathalie Gaillard ¹, Laure Bertry ², Reka Toth ³, Thierry Le Mercier ², Valérie Buissette ² and Marc Dubois ^{1,*} 

¹ Institut de Chimie de Clermont-Ferrand (UMR 6296), Université Clermont Auvergne, CNRS, BP 10448, F-63000 Clermont-Ferrand, France; michael.herraiz@uca.fr (M.H.); saida.moumen@doctorant.uca.fr (S.M.); kevin.lemoine@uca.fr (K.L.); laurent.jouffret@uca.fr (L.J.); katia.araujo_da_silva@uca.fr (K.G.); elodie.petit@uca.fr (E.P.); nathalie.gaillard@uca.fr (N.G.)

² Centre de Recherche & Innovation, Syensqo, 52 Rue de la Haie Coq, 93300 Aubervilliers, France; thierry.le-mercier@syensqo.com (T.L.M.); valerie.buissette@syensqo.com (V.B.)

³ Solvay, 9 rue des Cuirassiers, 69003 Lyon, France; reka.toth@solvay.com

* Correspondence: marc.dubois@uca.fr

Abstract

After reviewing the state of the art of the fluorination of inorganic solid electrolytes, an application of gas/solid fluorination is given and how it can be processed. Garnet-type oxide has been chosen. These oxides with an ideal structure of chemical formula $A_3B_2(XO_4)_3$ are mainly known for their magnetic and dielectric properties. Certain garnets may have a high enough Li^+ ionic conductivity to be used as solid electrolyte of lithium ion battery. The surface of LLZO may be changed in contact with the moisture and CO_2 present in the atmosphere that results in a change of the conductivity at the interface of the solid. $LiOH$ and/or lithium carbonate are formed at the surface of the garnet particles. In order to allow for handling and storage under normal conditions of this solid electrolyte, surface fluorination was performed using elemental fluorine. When controlled using mild conditions (temperature lower or equal to 200 °C, either in static or dynamic mode), the addition of fluorine atoms to LLZO with $Li_{6.4}Al_{0.2}La_3Zr_2O_{12}$ composition is limited to the surface, forming a covering layer of lithium fluoride LiF. The effect of the fluorination was evidenced by IR, Raman, and NMR spectroscopies. If present in the pristine LLZO powder, then the carbonate groups disappear. More interestingly, contrary to the pristine LLZO, the contents of these groups are drastically reduced even after storage in air up to 45 days when the powder is covered with the LiF layer. Surface fluorination could be applied to other solid electrolytes that are air sensitive.

Keywords: garnet-type oxides; lithium ion battery; solid electrolyte; fluorination; surface treatment

1. The State of the Art

The potential of solid electrolytes in the energy field for Li ion batteries (LiBs) has been the subject of considerable interest. This novel class of electrolytes has demonstrated a multitude of benefits for Li ion batteries, effectively circumventing a substantial challenge inherent to liquid electrolytes. One such issue is safety, given the flammable nature of the electrolyte used in Li ion batteries. Meanwhile, solid electrolytes have demonstrated considerable efficacy in limiting this issue by impeding the growth of Li dendrites on the Li anode [1,2]. Furthermore, solid electrolytes are distinguished by their high energy density



Academic Editors: Shaokun Chong and Jae-won Lee

Received: 23 May 2025

Revised: 7 July 2025

Accepted: 8 July 2025

Published: 16 July 2025

Citation: Herraiz, M.; Moumen, S.; Lemoine, K.; Jouffret, L.; Guérin, K.; Petit, E.; Gaillard, N.; Bertry, L.; Toth, R.; Le Mercier, T.; et al. Surface Fluorination for the Stabilization in Air of Garnet-Type Oxide Solid Electrolyte for Lithium Ion Battery. *Batteries* **2025**, *11*, 268. <https://doi.org/10.3390/batteries11070268>

Copyright: © 2025 by the authors. Licensee MDPI, Basel, Switzerland. This article is an open access article distributed under the terms and conditions of the Creative Commons Attribution (CC BY) license (<https://creativecommons.org/licenses/by/4.0/>).

and high ionic conductivity, which can approach that of liquid electrolytes [3,4]. A variety of solid electrolyte types have been developed and tested for use in LiBs. Notably, organic solid electrolytes utilizing polymers such as polyethylene oxide (PEO), polyacrylonitrile (PAN), polyethylene carbonate (PEC), polypropylene carbonate (PPC), and polymethyl methacrylate (PMMA) have been developed [5–7]. Furthermore, inorganic solid electrolytes are gaining popularity for use in LiBs due to their high ionic conductivities. This category encompasses numerous subcategories, including oxides such as LISICON, garnets LLMO ($M = Zr, Ta, Nb$), perovskites ABO_3 ($A = Li, Ca, Sr, La/B = Al$ or Ti), LIPON, LATP, and sulfides like thio-LISICON and argyrodites [8–11]. Each category offers valuable performance characteristics for LiBs. A third category of solid electrolytes has recently been developed, designated as hybrid solid electrolytes. The mixture comprises organic and inorganic materials, which are combined in order to take advantage of the characteristics of both [12–14]. Garnet-type oxides have an ideal structure with the chemical formula $A_3B_2(XO_4)_3$ and generally crystallize in a centered cubic lattice belonging to the $Ia\bar{3}d$ space group. The cationic sites A, B, and X have an oxygen coordination of VIII, VI, and IV, respectively. Synthetic garnets are mainly known for their magnetic and dielectric properties. However, it has been observed that some garnets can exhibit sufficiently high Li^+ ionic conductivity for use as solid electrolytes in lithium batteries [15–18]. In 2007, for example, teams succeeded in preparing a new garnet with the formula $Li_7La_3Zr_2O_{12}$ (LLZO) and achieved a total conductivity of the order of 3.10^{-4} S/cm [19]. Other studies have also shown that ionic conductivity is highest when the garnet has a cubic rather than a tetragonal structure. Other teams have shown that ionic conductivity is enhanced when the LLZO-type garnet includes another chemical element such as aluminum or niobium. Because of their high conductivity, LLZO-type garnets can be used as solid electrolytes in lithium batteries.

Despite the numerous advantages exhibited by solid electrolytes in Li ion batteries, there are certain properties that require further enhancement if solid electrolytes are to become the dominant technology in the field of energy storage. The use of solid electrolytes is constrained by several limitations, particularly in regard to their handling and the range of applications for which they are suitable. The surface of LLZO-type garnets can be modified by contact with moisture and CO_2 present in the atmosphere, leading to a drastic change in conductivity at the solid interface [16,20]. Indeed, $LiOH$ or lithium carbonate is observed to form on the surface of garnet particles when they are in contact with an ambient atmosphere [21]. It would therefore be useful to have garnets with a suitable ionic conductivity for use as a solid electrolyte in a lithium battery that can be stored and handled under normal conditions.

The most prevalent challenge associated with solid electrolytes pertains to their chemical, thermal, and electrochemical stability, which is largely attributed to interfacial side reactions [22–28]. The chemical stability of certain solid electrolytes may be compromised when they are exposed to ambient air. This reaction results in the degradation of the electrolyte, which manifests itself in various ways. For instance, sulfide solid electrolytes generate toxic gases such as hydrogen sulfide (H_2S) [22,29], while oxide solid electrolytes undergo a H^+ / Li^+ exchange [13,30]. Additionally, garnet-type LLZO electrolytes formed layers of impurities at the surface, including Li_2CO_3 and $LiOH$. It is therefore imperative that this type of electrolyte be handled in an inert environment [22,31]. Furthermore, electrochemical stability is a crucial property that must be evaluated. Some solid electrolytes exhibit a narrow electrochemical window or unstable interfaces between the electrolyte and the electrode, stemming from the formation of parasitic reactions at the interface during charge/discharge cycles [22,32]. Mechanically, properties of the material may be compromised by the formation of lithium dendrites, the development of cracks, and the

propagation of fractures [22,33]. Ultimately, thermal stability is a crucial factor in battery safety. During the cycling process, certain parasitic reactions may occur, resulting in the decomposition of the electrolyte and an increase in temperature. An increase in temperature can result in the decomposition of the electrolyte, which may subsequently lead to short circuits [22,34,35]. Therefore, solid electrolytes must possess sufficient thermal resistance of functioning under thermal conditions.

A novel strategy has recently been devised with the objective of enhancing the properties of solid electrolytes, with a particular focus on stability. The doping of materials has been identified as a means of enhancing the performance of batteries. Among the various doping types, fluorination, also known as halogenation, is worthy of particular mention. Fluorination can be defined as the introduction of fluorine ions into the structure of a solid electrolyte. Many research works have demonstrated the beneficial effects of fluorination on solid electrolytes. Indeed, the incorporation of fluorine ions results in the formation of a passivation layer of LiF at the interface between the solid electrolyte and the lithium anode [35,36]. This interface is designated the Solid Electrolyte Interface (SEI), and it plays a pivotal role in optimizing battery performance. The formation of this layer enables the blocking of lithium dendrite growth, thereby ensuring the longevity of batteries and preventing safety issues [37]. Moreover, numerous studies have demonstrated the distinction between solid electrolytes prior to and following fluorination. The formation of the LiF layer allows for the creation of a broad and stable electrochemical window following fluorination. The electrolyte structure's electrochemical stability under high voltages can be obtained by introducing fluorine, which is known for its strong oxidation resistance [38,39]. Solid electrolytes were more stable during battery cycling than normal electrolytes as was confirmed in many studies, such as the case of $\text{Li}_2\text{ZrCl}_{6-x}\text{F}_x$ [40], $\text{Li}_3\text{YBr}_{5.7}\text{F}_{0.3}$ [41], and more other electrolytes. Furthermore, the formation of the SEI layer provides protection for the solid electrolyte, which has beneficial mechanical properties due to the increased roughness and robustness of the layer [42]. Additionally, the fluorination of solid electrolytes enhances the ionic conductivity. As evidenced by the findings of Lu et al., the ionic conductivity of $\text{Li}_{6.25}\text{Ga}_{0.25}\text{La}_3\text{Zr}_2\text{O}_{12}$ (LGLZO) increased from $5.43 \times 10^{-4} \text{ S/cm}$ to $1.28 \times 10^{-3} \text{ S/cm}$ after fluorination [43].

The effect of surface fluorination was also investigated. Li et al. demonstrated that the introduction of LiF into LLZO increases the stability of the electrolyte against moisture and CO_2 . The LiF layer protects the LLZO garnet surface from the formation of Li_2CO_3 , hence the critical role of LiF in protecting the electrolyte surface [44], as well as enhancing interfacial reactions with lithium metal. This improves resistance to dendrite penetration and supports higher current densities without short circuiting [45]. It was also demonstrated that the fluorination of the electrode surface results in the formation of a passive layer of LiF at the interface. This layer played a pivotal role in stabilizing and protecting the electrolyte from decomposition [46,47]. Moreover, electrochemical characterization was conducted on LiF-coated Li metal and Li metal prior to fluorination. During the cycling process, the anode with the LiF coating demonstrated stability. However, the anode lacking LiF coating is not stable, and the formation of parasitic reactions on the surface results in short circuits [47]. Furthermore, the stabilizing effect of the LiF layer was also evident in other findings by fluorinating the surface of an anode material, $\text{Li}_4\text{Ti}_5\text{O}_{12}$. The formation of the LiF layer protected the anode surface from carbonates, reduced interfacial reactions between the electrode/electrolyte, and reduced the generation of gases like CO_2 during cycling [48]. These advantages were previously proven by fluorinating the surface of graphite anode for Li ion batteries. Surface analyses revealed a significant reduction in oxygen and hydrogen content, which positively impacts electrochemical performances by reducing unwanted side reactions [49]. The same benefits of the LiF layer were obtained

in the research works of Xiong et al. The formation of the LiF layer on the surface of the MXene/TiO₂ membrane was efficient in suppressing lithium dendrites and reinforcing the SEI [50].

Surface fluorination has emerged as a key technique to enhance the performance and durability of lithium ion battery (LiB) anodes and cathodes. For anodes, surface fluorination creates a protective lithium fluoride (LiF) layer that stabilizes the Solid Electrolyte Interphase (SEI), reduces side reactions, and prevents dendrite formation. Similarly, cathodes benefit from surface fluorination by improving interfacial stability, mitigating transition metal dissolution, and enhancing high-voltage cycling performance. Studies have demonstrated significant improvements in capacity retention and cycle life through controlled fluorination methodologies.

Surface fluorination typically involves gas/solid or plasma-assisted techniques using elemental fluorine (F₂) or fluorine-containing gases such as XeF₂. For example, the fluorination of LiNi_xCo_xMn_{1-2x}O₂ (NCM) cathodes at rates of 2–5 atomic percent has been shown to produce an optimal LiF layer, balancing protection and ionic conductivity. Similarly, fluorinated graphite anodes with coverage rates around 10–15% have demonstrated enhanced electrochemical stability [51]. These methodologies involve moderate temperatures (below 200 °C) to prevent bulk fluorination, which could degrade the underlying material structure. The fluorination of NCM cathodes has led to an increase in capacity retention by 20–30% over 500 cycles. Additionally, high-voltage cathodes such as LiCoO₂ (LCO) have shown improved performance, with a reduction in capacity fade by up to 50% due to the stabilizing LiF layer at the interface [52].

For graphite anodes, fluorination has reduced initial capacity losses by 15–25% while extending cycle life. The LiF layer formed during fluorination reduces the decomposition of organic electrolytes and enhances lithium ion transport through the SEI. The fluorination of SiO_x materials also leads to the formation of an LiF-rich SEI layer, which enhances the cycling stability of lithium ion batteries [53]. In the case of LTO, the surface fluorination of Li₄Ti₅O₁₂ (LTO) has been investigated by the decomposition of solid XeF₂ [54]. The surface fluorination of LTO passivates its surface, reducing side reactions with the electrolyte and improving the overall electrochemical stability. For instance, the fluorination process was found to influence the Ti⁴⁺ catalytic properties, thereby affecting gas formation within the cells. Surface fluorination did not alter the bulk structure of LTO but modified its surface reactivity, leading to enhanced electrochemical performance.

The aim of the present work is to provide a proof of concept of the surface fluorination applied to a solid electrolyte, i.e., garnets, without degrading their physicochemical properties. As a consequence, their ionic conductivity as a solid electrolyte in lithium batteries (not measured in the present work) is expected to be unchanged.

In practice, surface fluorination is not easy to achieve experimentally, as the active phase of LLZO (cubic structure) is extremely sensitive to processing conditions, as it is not thermodynamically stable at room temperature and is highly sensitive to humidity. Direct liquid fluorination would appear to be out of the question, hence the need to study the feasibility of gaseous fluorination. A heterogenous gas/solid fluorination with elemental fluorine (F₂) is considered. The gas/solid fluorination process using molecular fluorine is designed to be easy to implement without adding any material other than LiF in very small quantities. It therefore differs from alternative stabilization approaches such as ALD coating, ZrO₂ shell formation, or Li₃PO₄ interfacial layers requiring additives or complex methods.

2. A New Approach for the Stabilization of Inorganic Solid Electrolyte

2.1. Material

The garnet used is an Al-doped LLZO obtained by the method described in ref. [21,55]. The starting LLZO was obtained according to the 2-step procedure described in patent US20220278355. In brief, a La/Zr/Al precursor is first obtained by co-precipitation of nitrate salts with ammonia in water, followed by calcination in the presence of a templating agent. The precursor is then impregnated by a LiNO₃ aqueous solution and calcined successively at 900 °C and 1000 °C. The cations have the following relative composition determined by ICP: Li_{6.97}Al_{0.22}La₃Zr_{1.98}.

2.2. Fluorination

For the fluorination, 99.9% pure elemental fluorine (F₂) was used (with an HF impurity level < 0.5 vol% and an O₂/N₂ impurity of around 0.5 vol%). First of all, the reactivity of LLZO towards elemental fluorine was evaluated under an initial pressure of pure F₂ gas equal to 200 mbar. The pressure in the closed reactor (static mode) was controlled (Figure 1). After 200 mbar of fluorine gas was injected into the reactor without LLZO pressure initially under primary vacuum (10⁻³ mbar), the temperature increased in the system, resulting in a pressure increase. After this variation was demonstrated, the same experiment was carried out with LLZO (500 mg). The difference in terms of pressure evolution with and without LLZO was therefore related to the consumption of F₂ molecules or the decomposition of the sample with gas evolution. Here, for the same quantity of fluorine injected into the reactor, the response with the sample is slightly lower, giving the first indication of reactivity. The gas flows—both fluorine and inert gas for purging—are carefully controlled by mass flow controllers. Each fluorination experiment is repeated to ensure reproducibility, and pressure vs. time and pressure vs. temperature profiles are systematically compared across runs. Additionally, we have successfully scaled up the process from a few hundred milligrams to several grams of material without observing changes in air stability, confirming the robustness of the method.

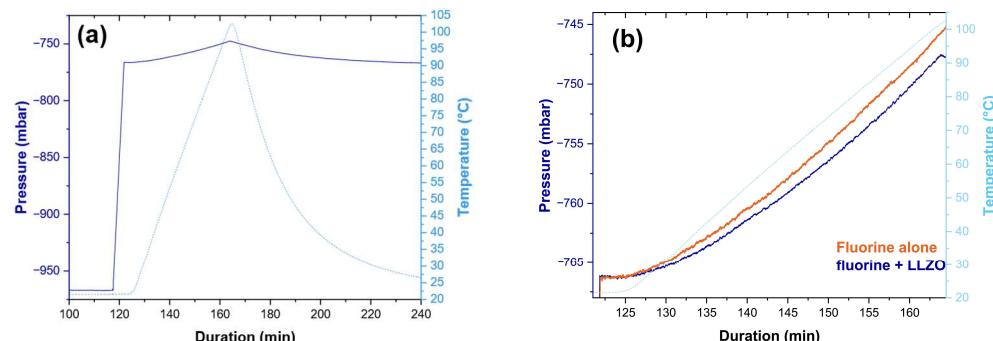


Figure 1. (a) Temperature and pressure curves for fluorine in the reactor as a function of time, and (b) zoom in on the difference in temperature behavior of fluorine with and without a sample.

In order to cover a wide range of fluorination conditions, several samples were treated:

- Static fluorination at room temperature (RT) with a F₂ pressure of 300 mbar for 1 h (**Stat-1 h**);
- Dynamic fluorination at RT for 1 h (**Dyn-1 h**);
- Dynamic fluorination at RT for 2 h (**Dyn-2 h**).

For each treatment, 500 mg of LLZO was deposited in a passivated nickel boat as a bed of powder with a thickness of less than 2 mm. The plate was inserted into the 1 L reactor at 25 °C. After the fluorination, the reactor was flushed with N₂ (50 mL/min) for an

hour and a half. When the temperature is different than room temperature, the reactor was left to cool freely under N₂ flux.

2.3. Physicochemical Characterization

Powder X-ray diffraction (XRD) patterns were obtained using a Malvern Panalytical Xpert Pro diffractometer equipped with a Cu source monochromated in the K α wavelength (1.541874 Å) with a K α_2 /K α_1 intensity ratio of 0.50. Scans were collected in the range of 10° to 90°, with a step size of 0.033° and counting time of 200 s. Diffraction patterns were analyzed using X'Pert HighScore Plus Software 4.9 [56].

Fourier-transform infrared (FTIR) spectra were recorded on a Nicolet 6700 FT-IR (Thermo scientific, Waltham, MA, USA) spectrometer in transmission mode at 4 cm⁻¹ resolution, and 256 scans were taken for each spectrum.

The samples were analyzed by Raman spectroscopy on a T64000 spectrometer from the company Jobin-Yvon (Edison, NJ, USA) equipped with a confocal microscope. The spectra were recorded after storing for 2 months in a sealed flask under ambient conditions. The incident laser used was an ionized argon solid laser operating at 532 nm. The incident power of the laser was 100 mW. The Raman analyses were carried out in the range of 250–1500 cm⁻¹ with acquisition times of 60 s for each window and a spectral width of 500 cm⁻¹, repeated twice.

Then, ¹⁹F and ⁷Li solid-state nuclear magnetic resonance (NMR) spectra were acquired on a Bruker AVANCE spectrometer where 2.5 zirconia rotors rotating at 30 kHz were used. For MAS (magic angle spinning) spectra, a simple sequence was performed with a single π/2 pulse length of 4.0 and 3.5 μs for ¹⁹F and ⁷Li, respectively. The ⁷Li NMR was performed at a frequency of 116.59 MHz and LiCl was used as the reference. The ¹⁹F NMR was carried out with a frequency of 282.2 MHz, and the spectra were externally referenced to CFCl₃. For the determination of the proportion of fluorine by NMR, poly(vinylidene fluoride) (PVDF SOLEF 1015/1001) was used as an internal standard. The quantification was carried out using a Bruker 400 MHz Avance Neo spectrometer equipped with a 1.9 mm probe.

For Scanning Electron Microscopy–Energy Dispersive Spectroscopy (SEM–EDS) analysis, the powder was embedded in a Epofix resin, which polymerized at room temperature over 24 h. After polymerization, the solid containing the LLZO powder undergoes a section on a microtome setup (Reichert and Jung Ultracut E model) under dry conditions, making the section of some solid particles accessible. Then, the surface of the preparation was treated by a platinum sputtering under secondary vacuum in a Cressington 208HR sputter coater. The deposited thickness was a few nanometers. The preparation was introduced in SEM FEG LEO 1525. SEM–EDS analysis was performed at 8 kV with diaphragm 60 μm and working distance 8.5 mm. The EDS spectrum was analyzed by an Oxford SDD 80 mm² detector X Max N cooled by Peltier effect. Data treatment was conducted under AZTEC software V4.4 after beam optimization on a silicon standard. Line profiles are acquired at magnification 2000 with 500 data points for a length that is typically 20 mm. Under these conditions at 8 kV, the analyzed volume was <1 μm³. The absolute intensity of the elements F (K lines) and La (M lines) was measured as a function of the position on the line profile.

For X-ray Photoelectron Spectroscopy (XPS), the powdered samples were pressed on an indium pellet. The XPS instrument was a THERMO K-alpha+ with a monochromatized AlK α X-ray source. The data treatment software was Avantage 3.1. The atomic concentrations are obtained from high-resolution spectra for each element. XPS analysis was conducted on samples as is and with Ar⁺ ions. In order to give an order of magnitude of the sputtered thickness, we referred to the sputtering rate of SiO₂ in the following results. The analytical and instrumental specifications were as follows: take-off angle of 90°, depth of analysis lower than 10 nm (average 3 nm), spot diameter of 400 μm, all elements were

detectable except H and He, sensitivity limits from 0.1% to 0.5 at., quantitative analysis with accuracy of 10 to 20%, and precision 2 to 5% (relative) depending on the concentration.

3. Results

3.1. Fluorination Is Limited to the Outmost Surface

To gain insight into the structure before and after fluorination, X-ray diffraction analyses of the powders were carried out (Figure 2). The overall structure of the sample appears unaffected by the treatment, with the same diffraction peaks, both in terms of width at half-height and position. Only a low-intensity peak can be observed for Dyn-2 h at 28° that could correspond to LaF_3 in a very small quantity.

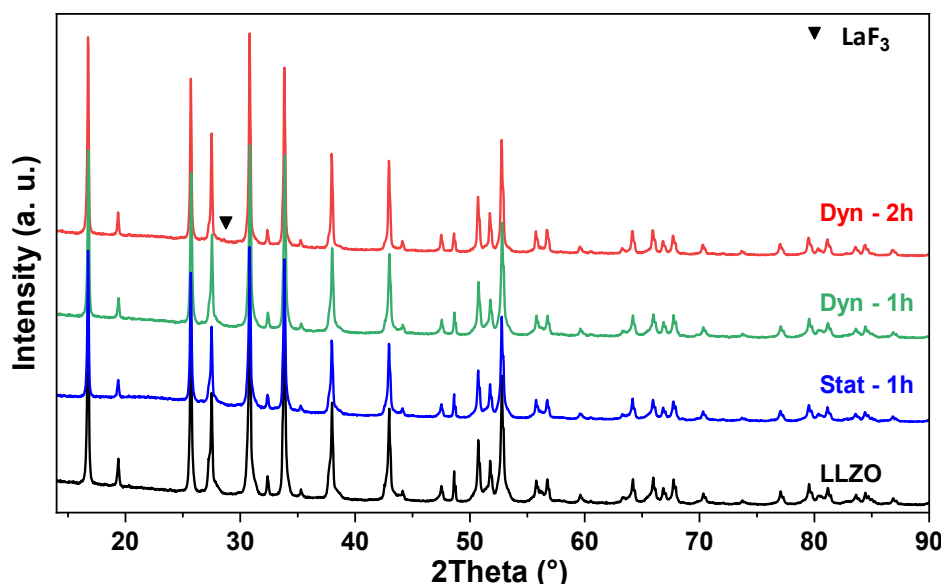


Figure 2. X-ray diffractograms of various LLZO powders fluorinated under different conditions; from top to bottom, Dyn-2 h, Dyn-1 h, Stat-1 h, and LLZO.

In view of this result, it is then necessary to resort to a characterization technique more suited to the detection of elements present in a matrix, in the case of the solid-state NMR study for the ^{19}F nucleus. As the initial compound does not contain fluorine, this element is only introduced through the process used. Solid-state NMR on ^{19}F nuclei is very useful, not only for highlighting the formation of LiF but also the destruction of the inorganic matrix. In this case, fluorides are formed, which cause resonance bands to appear in the NMR spectrum.

Figure 3a,b shows the solid-state NMR spectra of the samples for, respectively, the ^{19}F nucleus, synonymous with the presence of fluorine within the sample, in small quantities (number of pulses at least 128), and ^7Li . According to the band resonance, the symmetrical signal at $-204 \text{ ppm}/\text{CFCl}_3$ indicates the presence of Li-F bonds. Indeed, according to the XRD previously exploited, there is no formation of crystallized fluorinated phases visible in the results, which implies that the matrix has been fluorinated, in a partial way, without changing its structure. It is also interesting to note that for the longest dynamic fluorination time (2 h), additional bands appear (marked by red arrows). Given the very low fluorine content in **Stat-1 h**, the rotor signature can be seen (black arrow). These additional signals around -178 and -138 ppm reflect different environments for ^{19}F nuclei. Because of its proximity to the main LiF band, the one at -100 ppm may be an environment similar to that of LiF. This additional signature is only obtained for **Dyn-2 h**. A possible reactivity between lanthanum La and fluorine F would be visible by a resonance in the range of

[−30/−130 ppm], which is not necessarily visible in our case for all samples, with the exception of **Dyn-2 h**.

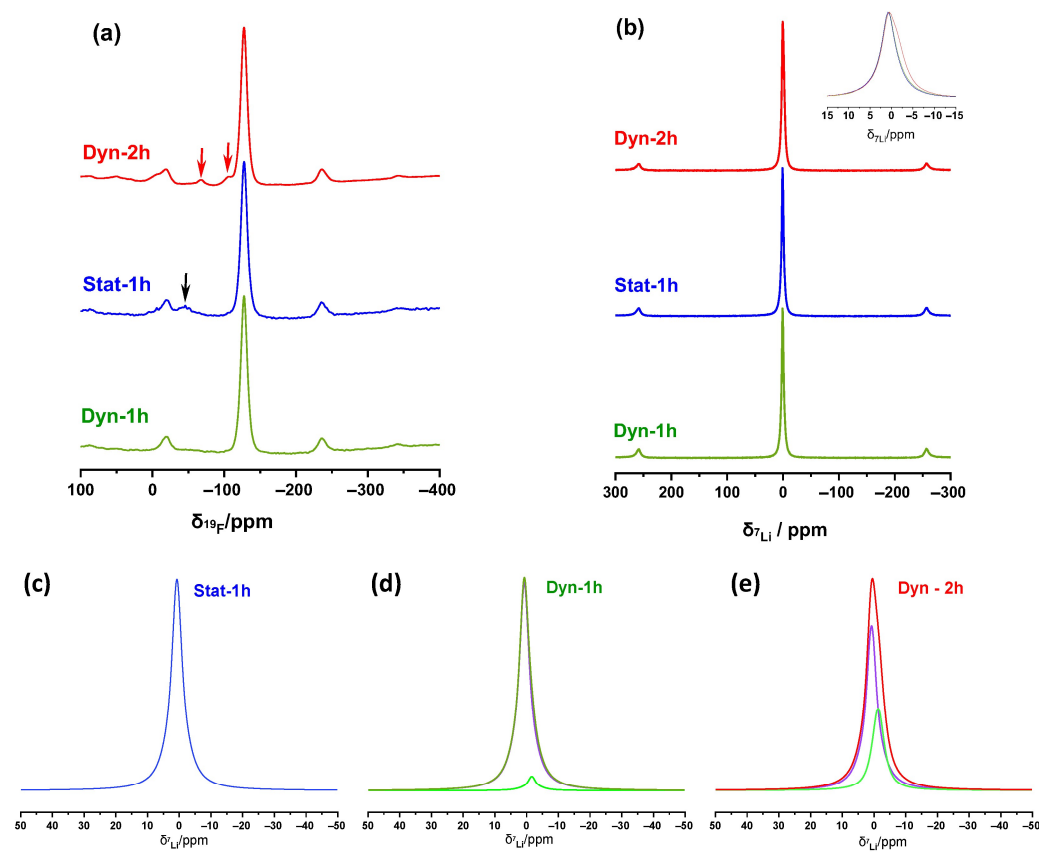


Figure 3. ^{19}F (a) and ^7Li (b) MAS NMR spectra (30 kHz) of LLZO fluorinated under different conditions: pulsed fluorination (20 mbar every 2 min/200 mbar total); static (300 mbar—1 h); dynamic fluorination (1 h); dynamic fluorination (2 h). (c–e) display the fits with Lorentzian lines of the ^7Li spectra.

The ^7Li spectra (Figure 3b) show a signal centered at around 0.7 ± 0.1 ppm. The fits of the spectra (Figure 3c–e) reveal two components for **Dyn-1 h** and **Dyn-2 h**, at 0.7 ± 0.1 ppm and 1.4 ± 0.1 ppm. In accordance with ^{19}F NMR data, this band is assigned to LiF. The second band at 0.74 ± 0.02 ppm is related to Li^+ of the LLZO lattice. The longer the dynamic fluorination duration, the higher the amount of LiF. As seen by ^{19}F NMR data, Lithium fluorine is also present in **Stat-1 h** but with very low content; the line is negligible in comparison with Li^+ in LLZO.

Previous results showed that, whatever the fluorination conditions, the LLZO structure was largely preserved, but that the fluorine reacted with the precursor, since the presence of Li-F was detected. The compound treated in dynamic mode for 2 h stood out for the presence of at least one additional minority phase.

Another issue is the instability in air of LLZO samples. Indeed, the product tends to undergo carbonation when stored under standard conditions. Once received, it was stored in a glove box, under an inert atmosphere, to preserve it and limit pollution before fluorination. It should be noted that fluorination is sometimes used to purify products, notably by degrading carbon layers on the surface through the formation of volatile fluorocarbons (CF_4).

Raman spectroscopy was used to monitor the presence of carbonate groups on the sample as a function of fluorination conditions. Figure 4 displays the evolution of the Raman response for samples **Dyn-1 h**, **Dyn-2 h**, and **Stat-1 h** in the $[250\text{--}1500\text{ cm}^{-1}]$ range. Initially, the spectra of raw and treated LLZO shows several common bands, evidencing the maintaining of the structure. The vibration band at 354 and 508 cm^{-1} are characteristic

of the deformation modes of the octahedral units based on ZrO_6^{2-} [22,57–63]. The band at 648 cm^{-1} is assigned to the stretching modes of these same units [64]. The band at 1080 cm^{-1} changes in intensity according to the fluorination conditions [65]. It is assigned to the vibration of C–O bonds of CO_3^{2-} carbonate groups ($A_{1''}$ symmetrical stretch) [57–59]. This band decreases in intensity for **Stat-1 h** and **Dyn-1 h** and even disappears for **Dyn-2 h**. These data confirm the phenomenon of carbonation once the material has been returned to air. After fluorination, the results demonstrate the benefits of fluorination, since the structure stabilizes as fluorination progresses, with almost total limitation of the phenomenon after 2 h of treatment in dynamic mode. It should be noted that the fluorinated sample **Dyn-2 h** was stored in air for almost 3 months. No carbonation was visible using Raman spectroscopy. Carbonate ions were removed from LLZO by prolonged fluorination (2 h).

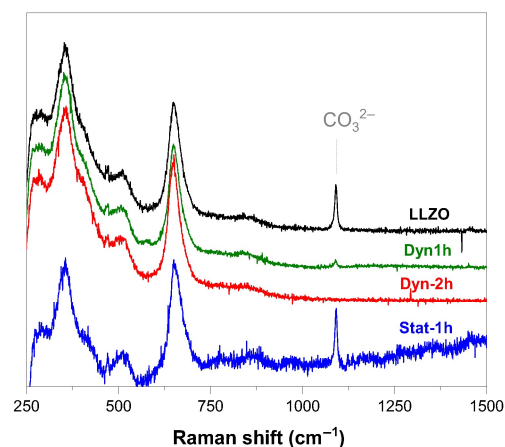


Figure 4. Raman spectra of fluorinated samples in dynamic (top) and static (bottom) modes.

To confirm LLZO decarbonation and stabilization, IR spectroscopy in ATR mode was carried out. The spectra are shown in Figure 5. The main vibrational modes are related to the carbonate ions E' asymmetric stretching and $A_{2''}$ out-of-plane bending at $1409\text{--}1460$ and 879 cm^{-1} , respectively [57,61,62,66]. These bands disappear almost completely for LLZO treated for 2 h in dynamic mode. The band at 846 and 680 cm^{-1} are assigned to lithium hydroxyl and water rocking vibrations, respectively. $\text{LiOH}\cdot\text{H}_2\text{O}$ forms on the surface, which is a necessary intermediate step for Li_2CO_3 formation [60,67]. The weak bands for LiOH and H_2O disappear only after long-term dynamic treatment. At this stage, the LiF layer is enough of a covering to block hydrolysis and subsequently the formation of Li_2CO_3 .

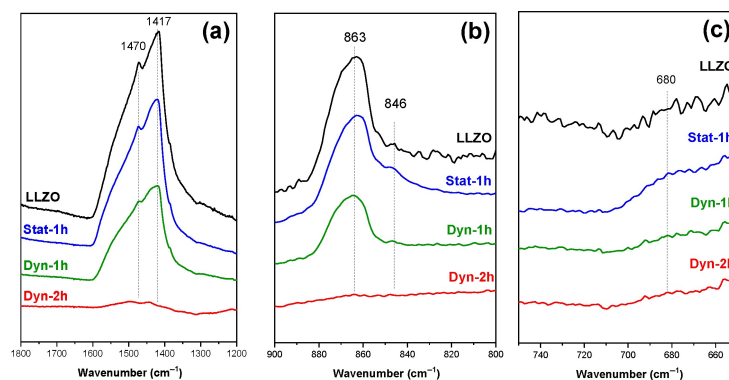


Figure 5. IR spectra (ATR mode) of fluorinated samples with dynamic and static modes in the $1200\text{--}1800$ (a), $800\text{--}900$ (b), and $650\text{--}750 \text{ cm}^{-1}$ range (c).

IR and Raman spectroscopies indisputably indicate carbonate removal and protection against LLZO carbonation by fluorination. Fluorination must be sufficiently long in dynamic mode (2 h with excess of F₂ gas) for the phenomena to be completed.

The results of SEM–EDS analysis as reported in Figure 6 evidence the distribution of fluorine and lanthanum elements along the section of fluorinated LLZO solid particles. The fluorine atoms are concentrated on the surface of the particles, while their core is lanthanum-rich. The ratio F/Zr from XPS were expressed in function of material depth. F/Zr is equal to 1.0, 0.7, and 0.3 at the surface, at 15 nm, and 50 nm from the surface, respectively.

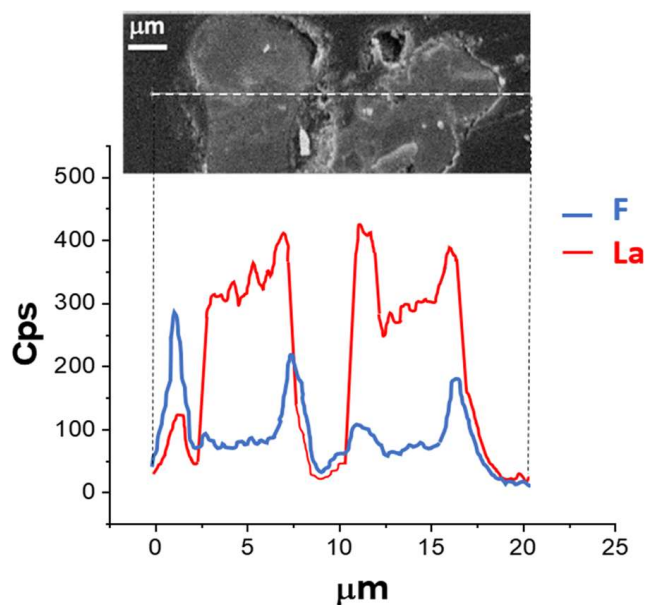


Figure 6. SEM–EDS analysis of Dyn-2 h.

Fluorination of LLZO results in a layer of LiF on the surface of the grain. This layer seems to be enough of a covering when the fluorination is performed for a long duration (2 h) in dynamic mode, i.e., with a continuous flux of F₂ molecules. The reaction with moisture and CO₂ from air is avoided thanks to this covering layer, which is evidenced in Figure 7.

Using PVDF SOLEF 1015/1001 as an internal standard for the quantification, the relative contents are 0.7, 3.3, and 0.9%F (by weight) for Dyn-1 h, Dyn-2 h, and Stat-1 h, respectively.

3.2. Fluorination Allows for Long-Term Stabilization

The air exposure-induced contamination impacts the interfacial resistance significantly when exposure time exceeds 24 h [22]. The following step was to investigate for how long the protection in air by fluorination is effective. The infrared spectra were recorded just after the fluorination t₀ and according to the time of air exposure up to 45 days (Figure 7). The intensity increases of all the vibration bands for carbonates started as soon as the exposure. The band at 1570 cm⁻¹ appears clearly only for the raw LLZO, especially after 11 days of exposure (Figure 7c); it can be assigned to symmetrical water H-O-H deformation [67]. On the contrary, all the vibration bands remained low-intensity for **Dyn-2 h**, whatever the air exposure duration. Only their wavenumbers are slightly shifted, i.e., 1437 and 1490 cm⁻¹ instead of 1417 and 1471 cm⁻¹ for the raw LLZO. The very weak band at 1572 cm⁻¹ is not shifted. The long-term (45 days) stability in air is significantly enhanced thanks to the fluorination for 2 h in dynamic mode. Nevertheless, the LiF coating may be not completely hermetic to moisture since the vibration bands in the ranges associated with carbonates and hydroxide groups are very weak but observable.

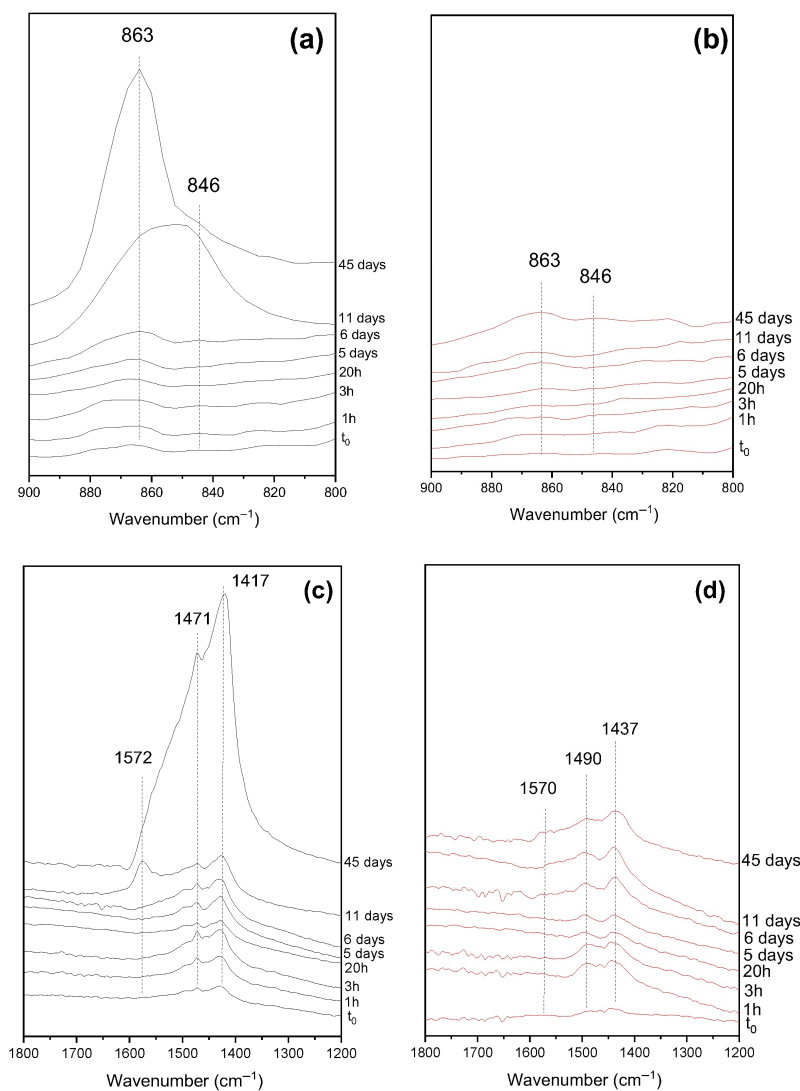


Figure 7. IR spectra (ATR mode) of raw LLZO (a,c) and Dyn-2 h (b,d) according to the time of exposure in air.

4. Conclusions and Perspectives

As the reactivity of LLZO with fluorine had never been demonstrated in the literature, several fluorination methods and conditions to quickly refocus the range were explored. Dynamic fluorination proved to be a serious option for purifying the precursor and stabilizing it under standard atmospheric conditions. Indeed, with the formation of carbonates as soon as the sample is exposed to air, precursor pollution can be reduced or even almost annihilated by dynamic fluorination, as shown by Raman and IR (ATR mode) spectroscopies. The structure appears intact after fluorination according to X-ray diffraction, but NMR spectroscopy for the ^{19}F and ^7Li nuclei shows the formation of Li-F or even a very few M-F bonds (M = La or Zr). Further analysis of the lithium will be useful to determine which atoms the fluorine has reacted with and whether the mobility of Li^+ ions is affected by the process. Because of the interest from an industrial standpoint to be able to handle the powder outside of a dry room for all stages prior to sintering, the surface fluorination of LLZO was carried out on the powder material. Nevertheless, the stability in air was only relevant for unpressed powders, as LLZO requires high-temperature annealing of 1000 °C to form a ceramic pellet with good conductivity. The maintaining of the LiF surface coating and its diffusion need to be evaluated. Moreover, the effect of surface fluorination on ionic conductivity as a solid electrolyte in lithium batteries must be investigated using

electrochemical impedance spectroscopy. To continue further in this process, the structure or porosity of the LiF layer requires study, especially during long-term operation. Finally, although ionic conductivity measurements are beyond the scope of the present work, it is essential to determine whether the improved air stability achieved through surface fluorination also enhances the electrochemical performance of LLZO.

Author Contributions: Conceptualization, M.D., K.L., L.J., K.G., M.H., L.B., R.T., T.L.M. and V.B.; methodology, M.D., K.L., L.J., K.G., M.H., L.B., R.T., T.L.M. and V.B.; formal analysis, M.H., M.D., K.L., L.J., E.P., N.G., S.M. and K.G.; data curation, M.H., M.D., K.L., L.J., E.P., N.G., S.M. and K.G.; writing—original draft preparation, M.D., K.L., L.J., K.G., L.B., R.T., T.L.M. and V.B.; writing—review and editing, M.D., K.L., L.J., S.M., K.G., L.B., R.T., T.L.M. and V.B.; visualization, supervision, M.D., K.L., L.J., K.G., L.B., R.T. and T.L.M.; project administration, M.D. and K.G.; funding acquisition, M.D. and K.G. All authors have read and agreed to the published version of the manuscript.

Funding: This research received funding from SYENSQO.

Data Availability Statement: Data is contained within the article.

Conflicts of Interest: Authors Laure Bertry, Thierry Le Mercier and Valérie Buissette were employed by the company Syensqo; Author Reka Toth was employed by the company Solvay. The remaining authors declare that the research was conducted in the absence of any commercial or financial relationships that could be construed as a potential conflict of interest.

References

- Cheng, X.-B.; Zhao, C.-Z.; Yao, Y.-X.; Liu, H.; Zhang, Q. Recent Advances in Energy Chemistry between Solid-State Electrolyte and Safe Lithium-Metal Anodes. *Chem.* **2019**, *5*, 74–96. [[CrossRef](#)]
- Meabe, L.; Aldalur, I.; Lindberg, S.; Arrese-Igor, M.; Armand, M.; Martinez-Ibañez, M.; Zhang, H. Solid-State Electrolytes for Safe Rechargeable Lithium Metal Batteries: A Strategic View. *Mater. Futures* **2023**, *2*, 33501. [[CrossRef](#)]
- Wang, C.; Wang, C.; Li, M.; Zhang, S.; Zhang, C.; Chou, S.; Mao, J.; Guo, Z. Design of Thin Solid-State Electrolyte Films for Safe and Energy-Dense Batteries. *Mater. Today* **2024**, *72*, 235–254. [[CrossRef](#)]
- Aurbach, D.; Talyosef, Y.; Markovsky, B.; Markevich, E.; Zinigrad, E.; Asraf, L.; Gnanaraj, J.S.; Kim, H.-J. Design of Electrolyte Solutions for Li and Li-Ion Batteries: A Review. *Electrochim. Acta* **2004**, *50*, 247–254. [[CrossRef](#)]
- Xi, G.; Xiao, M.; Wang, S.; Han, D.; Li, Y.; Meng, Y. Polymer-Based Solid Electrolytes: Material Selection, Design, and Application. *Adv. Funct. Mater.* **2021**, *31*, 2007598. [[CrossRef](#)]
- Chen, Z.; Kim, G.-T.; Wang, Z.; Bresser, D.; Qin, B.; Geiger, D.; Kaiser, U.; Wang, X.; Shen, Z.X.; Passerini, S. 4-V Flexible All-Solid-State Lithium Polymer Batteries. *Nano Energy* **2019**, *64*, 103986. [[CrossRef](#)]
- Mauger, A.; Julien, C.M. Solid Polymer Electrolytes for Lithium Batteries: A Tribute to Michel Armand. *Inorganics* **2022**, *10*, 110. [[CrossRef](#)]
- Manthiram, A.; Yu, X.; Wang, S. Lithium Battery Chemistries Enabled by Solid-State Electrolytes. *Nat. Rev. Mater.* **2017**, *2*, 16103. [[CrossRef](#)]
- Knauth, P. Inorganic Solid Li Ion Conductors: An Overview. *Solid State Ion.* **2009**, *180*, 911–916. [[CrossRef](#)]
- Zheng, F.; Kotobuki, M.; Song, S.; Lai, M.O.; Lu, L. Review on Solid Electrolytes for All-Solid-State Lithium-Ion Batteries. *J. Power Sources* **2018**, *389*, 198–213. [[CrossRef](#)]
- Zhao, N.; Khokhar, W.; Bi, Z.; Shi, C.; Guo, X.; Fan, L.-Z.; Nan, C.-W. Solid Garnet Batteries. *Joule* **2019**, *3*, 1190–1199. [[CrossRef](#)]
- Keller, M.; Varzi, A.; Passerini, S. Hybrid Electrolytes for Lithium Metal Batteries. *J. Power Sources* **2018**, *392*, 206–225. [[CrossRef](#)]
- Cheng, Z.; Liu, T.; Zhao, B.; Shen, F.; Jin, H.; Han, X. Recent Advances in Organic-Inorganic Composite Solid Electrolytes for All-Solid-State Lithium Batteries. *Energy Storage Mater.* **2021**, *34*, 388–416. [[CrossRef](#)]
- Bhardwaj, R.K.; Zitoun, D. Recent Progress in Solid Electrolytes for All-Solid-State Metal(Li/Na)–Sulfur Batteries. *Batteries* **2023**, *9*, 110. [[CrossRef](#)]
- Chen, R.; Li, Q.; Yu, X.; Chen, L.; Li, H. Approaching Practically Accessible Solid-State Batteries: Stability Issues Related to Solid Electrolytes and Interfaces. *Chem. Rev.* **2020**, *120*, 6820–6877. [[CrossRef](#)] [[PubMed](#)]
- Murugan, R.; Thangadurai, V.; Weppner, W. Fast Lithium Ion Conduction in Garnet-Type $\text{Li}_7\text{La}_3\text{Zr}_2\text{O}_{12}$. *Angew. Chemie Int. Ed.* **2007**, *46*, 7778–7781. [[CrossRef](#)] [[PubMed](#)]
- Ramakumar, S.; Janani, N.; Murugan, R. Influence of Lithium Concentration on the Structure and Li^+ Transport Properties of Cubic Phase Lithium Garnets. *Dalt. Trans.* **2015**, *44*, 539–552. [[CrossRef](#)] [[PubMed](#)]

18. Awaka, J.; Kijima, N.; Hayakawa, H.; Akimoto, J. Synthesis and Structure Analysis of Tetragonal $\text{Li}_7\text{La}_3\text{Zr}_2\text{O}_{12}$ with the Garnet-Related Type Structure. *J. Solid State Chem.* **2009**, *182*, 2046–2052. [[CrossRef](#)]
19. Thangadurai, V.; Kaack, H.; Weppner, W.J.F. Novel Fast Lithium Ion Conduction in Garnet-Type $\text{Li}_5\text{La}_3\text{M}_2\text{O}_{12}$ ($\text{M} = \text{Nb}, \text{Ta}$). *J. Am. Ceram. Soc.* **2003**, *86*, 437–440. [[CrossRef](#)]
20. Cheng, L.; Crumlin, E.J.; Chen, W.; Qiao, R.; Hou, H.; Franz Lux, S.; Zorba, V.; Russo, R.; Kostecki, R.; Liu, Z.; et al. The Origin of High Electrolyte–Electrode Interfacial Resistances in Lithium Cells Containing Garnet Type Solid Electrolytes. *Phys. Chem. Chem. Phys.* **2014**, *16*, 18294–18300. [[CrossRef](#)] [[PubMed](#)]
21. Cheng, L.; Park, J.S.; Hou, H.; Zorba, V.; Chen, G.; Richardson, T.; Cabana, J.; Russo, R.; Doeff, M. Effect of Microstructure and Surface Impurity Segregation on the Electrical and Electrochemical Properties of Dense Al-Substituted $\text{Li}_7\text{La}_3\text{Zr}_2\text{O}_{12}$. *J. Mater. Chem. A* **2014**, *2*, 172–181. [[CrossRef](#)]
22. Sharifi, A.; Yu, S.; Naguib, M.; Lee, M.; Ma, C.; Meyer, H.M.; Nanda, J.; Chi, M.; Siegel, D.J.; Sakamoto, J. Impact of Air Exposure and Surface Chemistry on Li– $\text{Li}_7\text{La}_3\text{Zr}_2\text{O}_{12}$ Interfacial Resistance. *J. Mater. Chem. A* **2017**, *5*, 13475–13487. [[CrossRef](#)]
23. Lim, H.-D.; Park, J.-H.; Shin, H.-J.; Jeong, J.; Kim, J.T.; Nam, K.-W.; Jung, H.-G.; Chung, K.Y. A Review of Challenges and Issues Concerning Interfaces for All-Solid-State Batteries. *Energy Storage Mater.* **2020**, *25*, 224–250. [[CrossRef](#)]
24. Janek, J.; Zeier, W.G. A Solid Future for Battery Development. *Nat. Energy* **2016**, *1*, 16141. [[CrossRef](#)]
25. Chen, Y.; Qian, J.; Li, L.; Wu, F.; Chen, R. Advances in Inorganic Solid-State Electrolyte/Li Interface. *Chem. A Eur. J.* **2024**, *30*, e202303454. [[CrossRef](#)] [[PubMed](#)]
26. Afyon, S.; Kravchyk, K.V.; Wang, S.; Broek, J.V.D.; Hänsel, C.; Kovalenko, M.V.; Rupp, J.L.M. Building Better All-Solid-State Batteries with Li-Garnet Solid Electrolytes and Metalloid Anodes. *J. Mater. Chem. A* **2019**, *7*, 21299–21308. [[CrossRef](#)]
27. Lou, S.; Zhang, F.; Fu, C.; Chen, M.; Ma, Y.; Yin, G.; Wang, J. Interface Issues and Challenges in All-Solid-State Batteries: Lithium, Sodium, and Beyond. *Adv. Mater.* **2021**, *33*, 2000721. [[CrossRef](#)] [[PubMed](#)]
28. Xu, R.C.; Xia, X.H.; Zhang, S.Z.; Xie, D.; Wang, X.L.; Tu, J.P. Interfacial Challenges and Progress for Inorganic All-Solid-State Lithium Batteries. *Electrochim. Acta* **2018**, *284*, 177–187. [[CrossRef](#)]
29. Muramatsu, H.; Hayashi, A.; Ohtomo, T.; Hama, S.; Tatsumisago, M. Structural Change of $\text{Li}_2\text{S}-\text{P}_2\text{S}_5$ Sulfide Solid Electrolytes in the Atmosphere. *Solid State Ion.* **2011**, *182*, 116–119. [[CrossRef](#)]
30. Simon, D.; Kelder, E.; Wagemaker, M.; Mulder, F.; Schoonman, J. Characterization of Proton Exchanged $\text{Li}_4\text{Ti}_5\text{O}_{12}$ Spinel Material. *Solid State Ion.* **2006**, *177*, 2759–2768. [[CrossRef](#)]
31. Samson, A.J.; Hofstetter, K.; Bag, S.; Thangadurai, V. A Bird’s-Eye View of Li-Stuffed Garnet-Type $\text{Li}_7\text{La}_3\text{Zr}_2\text{O}_{12}$ Ceramic Electrolytes for Advanced All-Solid-State Li Batteries. *Energy Environ. Sci.* **2019**, *12*, 2957–2975. [[CrossRef](#)]
32. Han, F.; Zhu, Y.; He, X.; Mo, Y.; Wang, C. Electrochemical Stability of $\text{Li}_{10}\text{GeP}_2\text{S}_{12}$ and $\text{Li}_7\text{La}_3\text{Zr}_2\text{O}_{12}$ Solid Electrolytes. *Adv. Energy Mater.* **2016**, *6*, 1501590. [[CrossRef](#)]
33. Famprikis, T.; Canepa, P.; Dawson, J.A.; Islam, M.S.; Masquelier, C. Fundamentals of Inorganic Solid-State Electrolytes for Batteries. *Nat. Mater.* **2019**, *18*, 1278–1291. [[CrossRef](#)] [[PubMed](#)]
34. Feng, X.; Ouyang, M.; Liu, X.; Lu, L.; Xia, Y.; He, X. Thermal Runaway Mechanism of Lithium Ion Battery for Electric Vehicles: A Review. *Energy Storage Mater.* **2018**, *10*, 246–267. [[CrossRef](#)]
35. von Aspern, N.; Röschenthaler, G.-V.; Winter, M.; Cekic-Laskovic, I. Fluorine and Lithium: Ideal Partners for High-Performance Rechargeable Battery Electrolytes. *Angew. Chemie Int. Ed.* **2019**, *58*, 15978–16000. [[CrossRef](#)] [[PubMed](#)]
36. Tan, J.; Matz, J.; Dong, P.; Shen, J.; Ye, M. A Growing Appreciation for the Role of LiF in the Solid Electrolyte Interphase. *Adv. Energy Mater.* **2021**, *11*, 2100046. [[CrossRef](#)]
37. Wang, T.; Duan, J.; Zhang, B.; Luo, W.; Ji, X.; Xu, H.; Huang, Y.; Huang, L.; Song, Z.; Wen, J.; et al. A Self-Regulated Gradient Interphase for Dendrite-Free Solid-State Li Batteries. *Energy Environ. Sci.* **2022**, *15*, 1325–1333. [[CrossRef](#)]
38. Tan, Y.-H.; Lu, G.-X.; Zheng, J.-H.; Zhou, F.; Chen, M.; Ma, T.; Lu, L.-L.; Song, Y.-H.; Guan, Y.; Wang, J.; et al. Lithium Fluoride in Electrolyte for Stable and Safe Lithium-Metal Batteries. *Adv. Mater.* **2021**, *33*, 2102134. [[CrossRef](#)] [[PubMed](#)]
39. Yang, F.; Liu, Y.; Liu, T.; Wang, Y.; Nai, J.; Lin, Z.; Xu, H.; Duan, D.; Yue, K.; Tao, X. Fluorinated Strategies Among All-Solid-State Lithium Metal Batteries from Microperspective. *Small Struct.* **2023**, *4*, 2200122. [[CrossRef](#)]
40. Ganesan, P.; Soans, M.; Cambaz, M.A.; Zimmermanns, R.; Gond, R.; Fuchs, S.; Hu, Y.; Baumgart, S.; Sotoudeh, M.; Stepien, D.; et al. Fluorine-Substituted Halide Solid Electrolytes with Enhanced Stability toward the Lithium Metal. *ACS Appl. Mater. Interfaces* **2023**, *15*, 38391–38402. [[CrossRef](#)] [[PubMed](#)]
41. Yu, T.; Liang, J.; Luo, L.; Wang, L.; Zhao, F.; Xu, G.; Bai, X.; Yang, R.; Zhao, S.; Wang, J.; et al. Superionic Fluorinated Halide Solid Electrolytes for Highly Stable Li-Metal in All-Solid-State Li Batteries. *Adv. Energy Mater.* **2021**, *11*, 2101915. [[CrossRef](#)]
42. Xu, R.; Zhang, X.-Q.; Cheng, X.-B.; Peng, H.-J.; Zhao, C.-Z.; Yan, C.; Huang, J.-Q. Artificial Soft–Rigid Protective Layer for Dendrite-Free Lithium Metal Anode. *Adv. Funct. Mater.* **2018**, *28*, 1705838. [[CrossRef](#)]
43. Lu, Y.; Meng, X.; Alonso, J.A.; Fernández-Díaz, M.T.; Sun, C. Effects of Fluorine Doping on Structural and Electrochemical Properties of $\text{Li}_{6.25}\text{Ga}_{0.25}\text{La}_3\text{Zr}_2\text{O}_{12}$ as Electrolytes for Solid-State Lithium Batteries. *ACS Appl. Mater. Interfaces* **2019**, *11*, 2042–2049. [[CrossRef](#)] [[PubMed](#)]

44. Li, Y.; Xu, B.; Xu, H.; Duan, H.; Lü, X.; Xin, S.; Zhou, W.; Xue, L.; Fu, G.; Manthiram, A.; et al. Hybrid Polymer/Garnet Electrolyte with a Small Interfacial Resistance for Lithium-Ion Batteries. *Angew. Chemie Int. Ed.* **2017**, *56*, 753–756. [[CrossRef](#)] [[PubMed](#)]
45. Dong, B.; Haworth, A.R.; Yeandel, S.R.; Stockham, M.P.; James, M.S.; Xiu, J.; Wang, D.; Goddard, P.; Johnston, K.E.; Slater, P.R. Halogenation of $\text{Li}_7\text{La}_3\text{Zr}_2\text{O}_{12}$ Solid Electrolytes: A Combined Solid-State NMR, Computational and Electrochemical Study. *J. Mater. Chem. A* **2022**, *10*, 11172–11185. [[CrossRef](#)]
46. Lin, D.; Liu, Y.; Chen, W.; Zhou, G.; Liu, K.; Dunn, B.; Cui, Y. Conformal Lithium Fluoride Protection Layer on Three-Dimensional Lithium by Nonhazardous Gaseous Reagent Freon. *Nano Lett.* **2017**, *17*, 3731–3737. [[CrossRef](#)] [[PubMed](#)]
47. Zhao, J.; Liao, L.; Shi, F.; Lei, T.; Chen, G.; Pei, A.; Sun, J.; Yan, K.; Zhou, G.; Xie, J.; et al. Surface Fluorination of Reactive Battery Anode Materials for Enhanced Stability. *J. Am. Chem. Soc.* **2017**, *139*, 11550–11558. [[CrossRef](#)] [[PubMed](#)]
48. Charles-Blin, Y.; Flahaut, D.; Guérin, K.; Dubois, M.; Monconduit, L.; Louvain, N.; Martinez, H. Surface Atomic Layer Fluorination of $\text{Li}_4\text{Ti}_5\text{O}_{12}$: Investigation of the Surface Electrode Reactivity and the Outgassing Behavior in LiBs. *Appl. Surf. Sci.* **2020**, *527*, 146834. [[CrossRef](#)]
49. Groult, H.; Nakajima, T.; Perrigaud, L.; Ohzawa, Y.; Yashiro, H.; Komaba, S.; Kumagai, N. Surface-Fluorinated Graphite Anode Materials for Li-Ion Batteries. *J. Fluor. Chem.* **2005**, *126*, 1111–1116. [[CrossRef](#)]
50. Xiong, C.; Wang, Z.; Peng, X.; Guo, Y.; Xu, S.; Zhao, T. Bifunctional Effect of Laser-Induced Nucleation-Preferable Microchannels and in Situ Formed LiF SEI in MXenes for Stable Lithium-Metal Batteries. *J. Mater. Chem. A* **2020**, *8*, 14114–14125. [[CrossRef](#)]
51. Bredemann, U.; Sicklinger, J.; Schipper, F.; Davis, V.; Fischer, A.; Huber, K.; Erickson, E.M.; Daub, M.; Hoffmann, A.; Erk, C.; et al. Fluorination of Ni-Rich Lithium-Ion Battery Cathode Materials by Fluorine Gas: Chemistry, Characterization, and Electrochemical Performance in Full-Cells. *Batter. Supercaps* **2021**, *4*, 632–645. [[CrossRef](#)]
52. Kim, S.; Kim, E.J.; Charles-Blin, Y.; Guérin, K.; Dubois, M.; Flahaut, D.; Martinez, H.; Deschamps, M.; Miller, D.N.; Irvine, J.T.S.; et al. Atomic Layer Fluorination of 5 V Class Positive Electrode Material LiCoPO_4 for Enhanced Electrochemical Performance. *Batter. Supercaps* **2020**, *3*, 1051–1058. [[CrossRef](#)]
53. Son, J.E.; Yim, J.-H.; Lee, J.-W. Fluorination of SiO_x as an Effective Strategy to Enhance the Cycling Stability of Lithium-Ion Batteries. *Electrochem. Commun.* **2023**, *152*, 107517. [[CrossRef](#)]
54. Charles-Blin, Y.; Flahaut, D.; Ledeuil, J.-B.; Guérin, K.; Dubois, M.; Deschamps, M.; Perbost, A.-M.; Monconduit, L.; Martinez, H.; Louvain, N. Atomic Layer Fluorination of the $\text{Li}_4\text{Ti}_5\text{O}_{12}$ Surface: A Multiprobing Survey. *ACS Appl. Energy Mater.* **2019**, *2*, 6681–6692. [[CrossRef](#)]
55. Le Mercier, T.; Braida, M.; Buissette, V.; Amisse, R.; Toth, R.; Bertry, L. Method of Preparation of a Garnet-Type Inorganic Material. Patent WO2021023599A1, 11 February 2021.
56. Degen, T.; Sadki, M.; Bron, E.; König, U.; Nénert, G. The HighScore Suite. *Powder Diffr.* **2014**, *29*, S13–S18. [[CrossRef](#)]
57. Neises, J.; Scheld, W.S.; Seok, A.-R.; Lobe, S.; Finsterbusch, M.; Uhlenbruck, S.; Schmeichel, R.; Benson, N. Study of Thermal Material Properties for Ta- and Al-Substituted $\text{Li}_7\text{La}_3\text{Zr}_2\text{O}_{12}$ (LLZO) Solid-State Electrolyte in Dependency of Temperature and Grain Size. *J. Mater. Chem. A* **2022**, *10*, 12177–12186. [[CrossRef](#)]
58. Jeong, W.; Park, S.S.; Yun, J.; Shin, H.R.; Moon, J.; Lee, J.-W. Tailoring Grain Boundary Structures and Chemistry of $\text{Li}_7\text{La}_3\text{Zr}_2\text{O}_{12}$ Solid Electrolytes for Enhanced Air Stability. *Energy Storage Mater.* **2023**, *54*, 543–552. [[CrossRef](#)]
59. Tsai, C.-L.; Ma, Q.; Dellen, C.; Lobe, S.; Vondahlen, F.; Windmüller, A.; Grüner, D.; Zheng, H.; Uhlenbruck, S.; Finsterbusch, M.; et al. A Garnet Structure-Based All-Solid-State Li Battery without Interface Modification: Resolving Incompatibility Issues on Positive Electrodes. *Sustain. Energy Fuels* **2019**, *3*, 280–291. [[CrossRef](#)]
60. Xia, W.; Xu, B.; Duan, H.; Tang, X.; Guo, Y.; Kang, H.; Li, H.; Liu, H. Reaction Mechanisms of Lithium Garnet Pellets in Ambient Air: The Effect of Humidity and CO₂. *J. Am. Ceram. Soc.* **2017**, *100*, 2832–2839. [[CrossRef](#)]
61. Zhang, Z.; Zhang, L.; Liu, Y.; Wang, H.; Yu, C.; Zeng, H.; Wang, L.; Xu, B. Interface-Engineered $\text{Li}_7\text{La}_3\text{Zr}_2\text{O}_{12}$ -Based Garnet Solid Electrolytes with Suppressed Li-Dendrite Formation and Enhanced Electrochemical Performance. *ChemSusChem* **2018**, *11*, 3774–3782. [[CrossRef](#)] [[PubMed](#)]
62. Mohammadi, S.; Golmohammad, M.; SharifiRad, A.; Alizadeh, S.M. Surface Modification and Chemical Stability of Garnet LLZO Solid Electrolyte by ZnO Coating through a Facile and Practical Method. *Mater. Chem. Phys.* **2023**, *308*, 128235. [[CrossRef](#)]
63. Scheld, W.S.; Collette, Y.; Schwab, C.; Ihrig, M.; Uhlenbruck, S.; Finsterbusch, M.; Fattakhova-Rohlfing, D. Ga-Ion Migration during Co-Sintering of Heterogeneous Ta- and Ga-Substituted LLZO Solid-State Electrolytes. *J. Eur. Ceram. Soc.* **2025**, *45*, 116936. [[CrossRef](#)]
64. Zhu, Y.; Chon, M.; Thompson, C.V.; Rupp, J.L.M. Time-Temperature-Transformation (TTT) Diagram of Battery-Grade Li-Garnet Electrolytes for Low-Temperature Sustainable Synthesis. *Angew. Chemie Int. Ed.* **2023**, *62*, e202304581. [[CrossRef](#)] [[PubMed](#)]
65. Liu, M.; Zhang, M.; Liu, S.; Chen, H.; Li, B.; Li, G.; Zhang, S.; Wen, Y.; Qiu, J.; Chen, J.; et al. Direct Wetting of $\text{Li}_7\text{La}_3\text{Zr}_2\text{O}_{12}$ Electrolyte with Molten Li Anode and Its Application in Solid-State Lithium Batteries. *J. Power Sources* **2024**, *593*, 233977. [[CrossRef](#)]

66. Sun, J.; Zhao, N.; Li, Y.; Guo, X.; Feng, X.; Liu, X.; Liu, Z.; Cui, G.; Zheng, H.; Gu, L.; et al. A Rechargeable Li-Air Fuel Cell Battery Based on Garnet Solid Electrolytes. *Sci. Rep.* **2017**, *7*, 41217. [[CrossRef](#)] [[PubMed](#)]
67. Gennick, I.; Harmon, K.M. Hydrogen Bonding. VI. Structural and Infrared Spectral Analysis of Lithium Hydroxide Monohydrate and Cesium and Rubidium Hydroxide Hydrates. *Inorg. Chem.* **1975**, *14*, 2214–2219. [[CrossRef](#)]

Disclaimer/Publisher’s Note: The statements, opinions and data contained in all publications are solely those of the individual author(s) and contributor(s) and not of MDPI and/or the editor(s). MDPI and/or the editor(s) disclaim responsibility for any injury to people or property resulting from any ideas, methods, instructions or products referred to in the content.